



OPEN

Understanding the effect of Mn^{2+} on $\text{Yb}^{3+}/\text{Er}^{3+}$ co-doped NaYF_4 upconversion and obtaining the optimal combination of these tridoping

Reza Zarei Moghadam^{1,3}✉, Hamid Rezagholipour Dizagi², Hans Agren³ & Mohammad Hossein Ehsani²✉

In this work, we investigated in detail the upconversion properties of several types of nanoparticles, including $\text{NaYF}_4:5\%\text{Yb}^{3+}/30\%\text{Mn}^{2+}$, $\text{NaYF}_4:40\%\text{Mn}^{2+}/x\%\text{Yb}^{3+}$ ($x\% = 1, 5, 10, 20, 30$, and 40), $\text{NaYF}_4:2\%\text{Er}^{3+}/x\%\text{Mn}^{2+}$ ($x\% = 20, 30, 40, 50, 60$, and 70), $\text{NaYF}_4:40\%\text{Mn}^{2+}/x\%\text{Er}^{3+}$ ($x\% = 1, 2, 5$, and 10), and $\text{NaYF}_4:40\%\text{Mn}^{2+}/1\%\text{Yb}^{3+}/x\%\text{Er}^{3+}$ ($x\% = 0, 2, 5$, and 10). We studied their upconversion emission under 980 nm excitation in both pulsed and continuous wave modes at different synthesis temperatures. The nanoparticles were characterized using transmission electron microscopy (TEM), X-ray diffraction (XRD), and photoluminescence (PL) spectroscopy. The doping of Yb^{3+} and Mn^{2+} ions resulted in the nanoparticles assuming cubic and hexagonal crystal structures. The emission intensity increased (106.4 (a.u. $\cdot 10^3$) to 334.4 (a.u. $\cdot 10^3$)) with increasing synthesis temperature from 120 to 140 °C, while a sharp decrease was observed when the synthesis temperature was increased to 200 °C. The gradual decrease in peak intensity with increasing Mn^{2+} concentration from 20 to 70% was attributed to energy transfer from Mn^{2+} to Yb^{3+} . In $\text{NaYF}_4:\text{Mn}^{2+}/\text{Yb}^{3+}/\text{Er}^{3+}$ UCNPs, increasing the Er^{3+} concentration from 0 to 10% led to the disappearance of the blue, orange, and green emission bands. The intense upconversion luminescence pattern with high spatial resolution indicates excellent potential for applications in displays, biological sensors, photodetectors, and solar energy converters.

Upconversion nanoparticles (UCNPs) possess a range of useful properties, such as low auto-fluorescence from cells, high penetration depth of light, high sensitivity for detection, sharp emission bandwidth, and large anti-Stokes shifts^{1–7}, which make them valuable for applications in biological, therapeutic, photonics, and other areas^{8–11}. UCNPs typically consist of two types of lanthanide (Ln) dopants, sensitizers and activators, immersed in an inorganic host lattice¹². Rare-earth (RE) ion-doped UCNPs have attracted increasing interest due to their broad potential applications and unique upconversion (UC) luminescence properties. Specifically, RE-doped UCNPs can convert spectral energy in the infrared, visible, or UV ranges^{13–15}.

Sodium yttrium fluoride (NaYF_4) is one of the most efficient host materials for red, green, and blue UC phosphors¹⁶. Nanoparticles of NaYF_4 exist in two structures: hexagonal and cubic, with the hexagonal form typically prepared by a high-energy consumption method at relatively high temperatures and the cubic form prepared by hydrothermal and solvothermal methods at relatively low temperatures¹⁷. NaYF_4 has often been applied as a doping host for Ln sensitizers and activators due to its low energy modes ($< 400/\text{cm}^{-1}$)¹⁸. Among the Er^{3+} ($^2\text{H}_{11/2}/^4\text{S}_{3/2}$), Tm^{3+} ($^3\text{F}_{2/3}/^3\text{H}_4$), Pr^{3+} ($^3\text{P}_1/^3\text{P}_0$), Eu^{3+} ($^5\text{D}_1/^5\text{D}_0$), Dy^{3+} ($^4\text{I}_{15/2}/^4\text{F}_{9/2}$), and Nd^{3+} ($^4\text{F}_{5/2}/^4\text{F}_{3/2}$) ions that often employed, Er^{3+} -doped NaYF_4 is recognized as one of the most stable UCNPs upon near-infrared light (NIR) excitations^{19–26}. More recently, the incorporation of divalent manganese (Mn^{2+}) ions has been recognized to decrease the short-wavelength green emission and increase the long-wavelength red emission due to energy transfer between the RE (often Er^{3+}) and Mn^{2+} ions²⁷. The Mn^{2+} emission bands, depending on the host surroundings, reside in the region of about 460 – 700 nm²⁸. Previous studies have demonstrated that doping NaYF_4

¹Department of Physics, Faculty of Science, Arak University, Arak 38156-88349, Iran. ²Faculty of Physics, Semnan University, P.O. Box: 35195-363, Semnan, Iran. ³Department of Theoretical Chemistry and Biology, KTH Royal Institute of Technology, 10691 Stockholm, Sweden. ✉email: r.zarei1991@gmail.com; ehsani@semnan.ac.ir

with Mn^{2+} ions can lead to strong red fluorescence in UCNPs, making them useful for *in vivo* imaging and drug delivery²⁹.

In this paper, we aim to shed further light on this mechanism by investigating the upconversion properties of several types of nanoparticles, including $\text{NaYF}_4:5\%\text{Yb}^{3+}/30\%\text{Mn}^{2+}$ at different synthesis temperatures, $\text{NaYF}_4:40\%\text{Mn}^{2+}/x\%\text{Yb}^{3+}$ ($x = 1, 5, 10, 20, 30, \text{ and } 40$), $\text{NaYF}_4:2\%\text{Er}^{3+}/x\%\text{Mn}^{2+}$ ($x = 20, 30, 40, 50, 60, \text{ and } 70$), $\text{NaYF}_4:40\%\text{Mn}^{2+}/x\%\text{Er}^{3+}$ ($x = 1, 2, 5, \text{ and } 10$), and $\text{NaYF}_4:40\%\text{Mn}^{2+}/1\%\text{Yb}^{3+}/x\%\text{Er}^{3+}$ ($x = 0, 2, 5, \text{ and } 10$) nanoparticles under 980 nm excitation in both pulsed and continuous wave modes. We characterized these nanoparticles using transmission electron microscopy (TEM), X-ray diffraction (XRD), and photoluminescence (PL) spectroscopy.

Previous studies have demonstrated that the doping of Mn^{2+} can decrease the non-radiative transition probability, thus improving the intensity of UCNP emission^{30–32}. Additionally, among UC materials, α -phase NaYF_4 is reported as one of the most efficient hosts for enhancing near-infrared (NIR) to single-red band up-conversion when tri-doped with $\text{Yb}^{3+}/\text{Er}^{3+}/\text{Mn}^{2+}$ ions³³. It has also been demonstrated that other nanosystems, including $\text{NaLuF}_4:\text{Yb}^{3+}/\text{Er}^{3+}/\text{Mn}^{2+}$, $\text{MnF}_2:\text{Yb}^{3+}/\text{Er}^{3+}$, and $\text{KMnF}_3:\text{Yb}^{3+}/\text{Er}^{3+}$, are effective emitters³⁴.

In our study, we investigated the upconversion properties of several types of UCNPs to better understand the energy transfer mechanisms among $\text{Yb}^{3+}/\text{Mn}^{2+}$, $\text{Mn}^{2+}/\text{Er}^{3+}$, and $\text{Mn}^{2+}/\text{Er}^{3+}/\text{Yb}^{3+}$ ions. We found that NaYF_4 is an efficient host material for red, green, and blue UC phosphors with cubic and hexagonal structures. Er^{3+} -doped NaYF_4 is recognized as one of the most stable UCNPs upon NIR excitations, while Mn^{2+} -doped NaYF_4 can lead to strong red fluorescence in UCNPs. Our results suggest that the doping of Mn^{2+} can decrease the non-radiative transition probability, thus improving the intensity of UCNP emission.

Overall, our findings help to shed further light on the energy transfer mechanisms in UCNPs and highlight the potential applications of these materials in various fields, such as biological sensing, photonics, and solar energy conversion.

Experiment

Materials

Yttrium (III) chloride hexahydrate ($\text{YCl}_3 \cdot 6\text{H}_2\text{O}$, 99.99%), Erbium (III) chloride hexahydrate ($\text{ErCl}_3 \cdot 6\text{H}_2\text{O}$, 99.99%), Ytterbium (III) chloride hexahydrate ($\text{YbCl}_3 \cdot 6\text{H}_2\text{O}$, 99.99%), Manganese (II) chloride hexahydrate ($\text{MnCl}_2 \cdot 6\text{H}_2\text{O}$, 99.99%), Sodium hydroxide (NaOH), oleic acid (OA), ammonium fluoride (NH_4F), ethanol (pure: 99.9), and cyclohexane were purchased from Sigma-Aldrich company. All chemicals were used as received without further purification.

Nanoparticle synthesis

Synthesis of $\text{NaYF}_4:5\%\text{Yb}^{3+}/30\%\text{Mn}^{2+}$ nanoparticles

Yb^{3+} and Mn^{2+} co-doped NaYF_4 nanoparticles were synthesized using a well-established hydrothermal method. NaOH (0.2 M, 1.2 ml) was added to a 50 ml centrifuge tube and stirred for 10 min. A mixture of ethanol (5 ml) and OA (5 ml) was added to NaOH and magnetically stirred for 15 min at room temperature until the solution became uniform and clear. A Ln solution was added to the centrifuge tube (Ln in total is 0.4 mmol): YCl_3 (0.26 mmol), YbCl_3 (0.02 mmol) and MnCl_2 (0.12 mmol). The solution was kept under magnetic stirring for 15 min. Subsequently, 59.26 mg of NH_4F dissolved in 1.6 ml of deionized water was added to the solution. The final solution was stirred magnetically for 1 h at a temperature of 40 °C. Thereafter, the solution was transferred into a Teflon (PTFE) reactor and sealed with Argon (Ar) gas. The PTFE reactor was inserted into an autoclave and heated at 120 °C, 140 °C, 160 °C, 180 °C, and 200 °C for 8 h. After 8 h, the autoclave was emptied, and the material in the PTFE reactor was cooled to room temperature. The solution was precipitated with ethanol (20 ml), collected by centrifugation (temperature: room temperature, time: 5 min, spin speed: 7500 rpm) washed several times with ethanol (10 ml), and dispersed in cyclohexane (10 ml) for further characterization. Further details of the synthesis of nanoparticles are given in the supplementary file.

Characterization

The size, shape, structure, and morphological characterization of the as-prepared UCNPs were characterized using a transmission electron microscope (TEM, JEOL, JEM-1400). The optical absorption spectrum in the wavelength range of 300–1000 nm was measured using an Edinburgh FS5 spectrophotometer. UC luminescence (UCL) spectra and decay curves were obtained using an Edinburgh FS5 spectrophotometer equipped with a 980 nm diode laser, operating in pulsed and continuous-wave (CW) mode. The pulse duration for the impact mode was 3 min, the power density of the 980 nm laser was 1 W/cm², and the spot width was 3 mm. 1000 μl of the solution was poured into the cuvette and the cuvette was placed inside the measuring device.

Results and discussion

Structure and morphology characterization

TEM was used to characterize the morphologies of the as-prepared UCNPs. Figure 1 displays TEM images of non-doped NaYF_4 UCNPs and $\text{NaYF}_4:30\%\text{Mn}^{2+}, 5\%\text{Yb}^{3+}$ UCNPs at various synthesis temperatures (120 °C, 140 °C, 160 °C, 180 °C, and 200 °C). The non-doped NaYF_4 UCNP crystal structure appeared completely hexagonal, while with the addition of Yb^{3+} and Mn^{2+} ions as dopants, the nanoparticles exhibited both cubic and hexagonal crystal structures. The average width of the nanoparticles was determined using the Digimizer software (version 4.1.1.0, MedCalc software) (Fig. 1), and only a minor dispersion of the nanoparticles' diameters was observed. To estimate the mean diameter of the nanoparticles, the obtained data were fitted with the Log-Normal distribution equation³⁵.

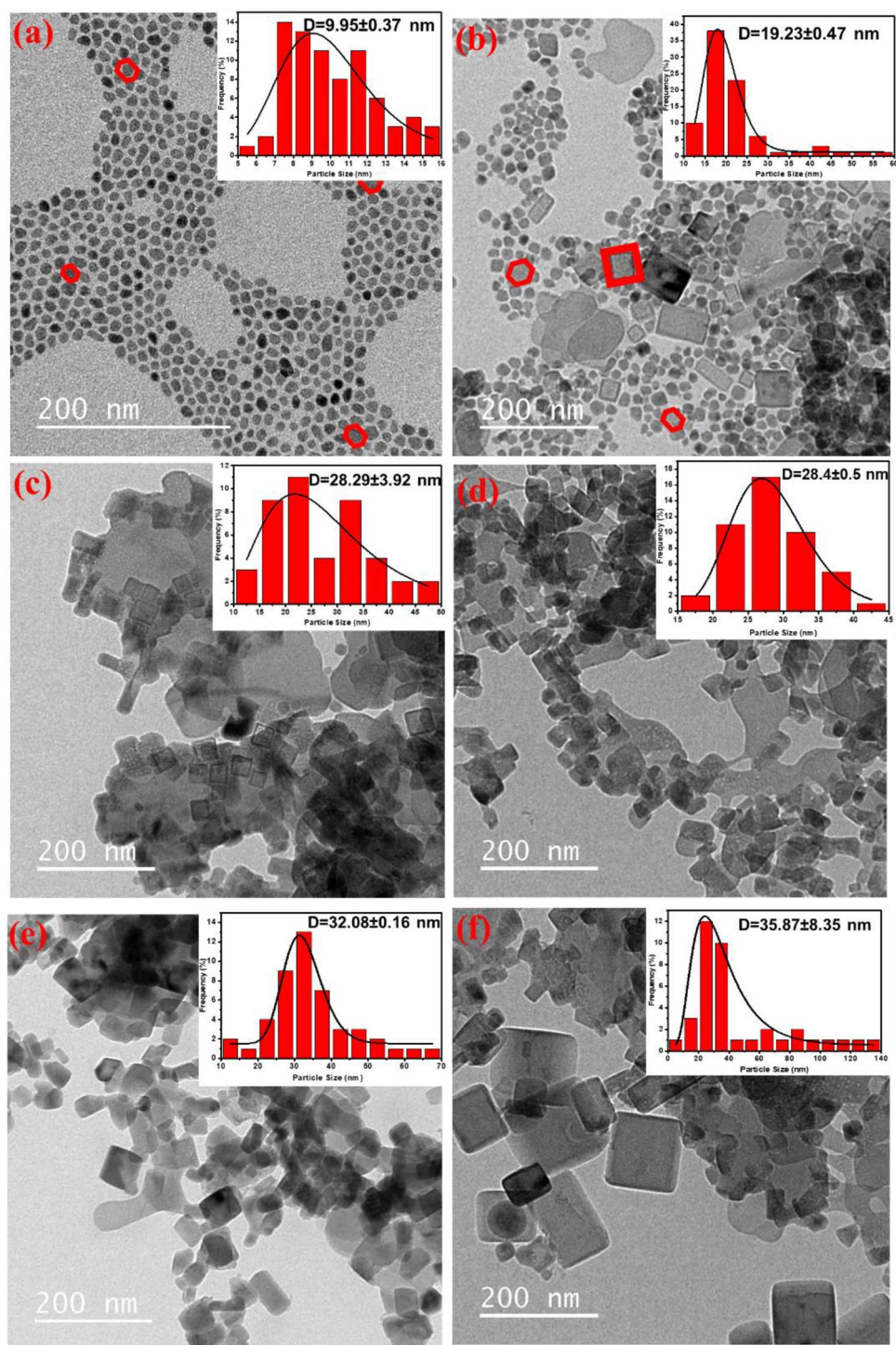


Figure 1. TEM images of the as-synthesized (a) NaYF₄, (b) 30%Mn 5%Yb 120 °C, (c) 30%Mn 5%Yb 140 °C, (d) 30%Mn 5%Yb 160 °C, (e) 30%Mn 5%Yb 180 °C, and (f) 30%Mn 5%Yb 200 °C. The analyzed samples were in solution form.

$$f(D) = \left(\frac{1}{\sqrt{2\pi}\sigma D} \right) \exp \left[-\frac{\ln^2\left(\frac{D}{D_0}\right)}{2\sigma^2} \right] \quad (1)$$

$$\langle D \rangle = D_0 \exp\left(\frac{\sigma^2}{2}\right) \quad (2)$$

$$\sigma_D = \langle D \rangle [\exp(\sigma^2) - 1]^{1/2} \quad (3)$$

Equations (1–3) were used to fit the data and obtain the fitting parameters D_0 and σ . Additionally, the standard deviation (σ_D) and mean diameter of the nanoparticles $\langle D \rangle$ were calculated using the results obtained from the data fitting. As shown in Fig. 1, the diameter of the nanoparticles increased from 19 to 36 nm as the temperature increased from 120 to 200 °C.

The TEM micrographs in Fig. 2 reveal that the $\text{NaYF}_4:5\% \text{Yb}^{3+}/x\% \text{Mn}^{2+}$ ($x = 30, 40, 50, 60, 70$) nanoparticles are polyhedral in shape with a uniform size. The average diameter of the $\text{NaYF}_4:5\% \text{Yb}^{3+}/x\% \text{Mn}^{2+}$ ($x = 30, 40, 50, 60, \text{ and } 70$) nanoparticles was found to be 28 nm. These results suggest that the crystal size of the nanoparticles increases and undergoes continuous and regular changes with the increase in Mn^{2+} content. As Mn^{2+} concentration increases from 30 to 70%, the number and size of the nanoparticles increases, as calculated using Eq. (2). The data demonstrate that the size of the nanoparticles increases from 21 to 30 nm as the Mn^{2+} concentration increases from 30 to 70%. Figure 2 also shows the appearance of several hexagonal hollow nanoparticles as Mn^{2+} concentration increases up to 70%. These observations are consistent with earlier reports^{36,37}.

The crystal structure and purity of $\text{NaYF}_4:5\% \text{Yb}^{3+}/30\% \text{Mn}^{2+}$ UCNPs were studied by analyzing the powder X-ray diffraction (XRD) patterns at different synthesis temperatures. Figure 3a displays XRD patterns of $\text{NaYF}_4:5\% \text{Yb}^{3+}/30\% \text{Mn}^{2+}$ UCNPs at different synthesis temperatures (120 °C, 140 °C, 160 °C, 180 °C, 200 °C). The XRD patterns of samples prepared at different synthesis temperatures (120 °C, 140 °C, 160 °C, 180 °C, 200 °C) indicate a mixed-phase NaYF_4 crystal, in agreement with standard patterns of cubic (JCPDS: 00-021-0547) and hexagonal (JCPDS: 00-016-0334). The results demonstrate that increasing the synthesis temperature from 120 to 200 °C leads to an increase in the cubic NaYF_4 phase peaks and crystallinity, which is consistent with the TEM images. Additionally, the zoomed image (Fig. 3a) shows that when the synthesis temperature is increased to 200 °C, the diffraction peak (111) slightly shifts to the lower-angle side, which can be attributed to the substitution of Y^{3+} ions by smaller Mn^{2+} ions in the host lattice³⁶. Figure 3b shows the XRD patterns of $\text{NaYF}_4:5\% \text{Yb}^{3+}/x\% \text{Mn}^{2+}$ ($x = 30, 40, 50, 60, 70$) UCNPs. The XRD patterns indicate a mixed-phase NaYF_4 crystal and are consistent with the standard patterns of cubic (JCPDS: 00-021-0547) and hexagonal (JCPDS: 00-016-0334) phases. When the concentration of Mn^{2+} is increased from 30 to 40%, the XRD pattern shows a cubic NaYF_4 phase. However, when the concentration of Mn^{2+} is further increased from 40 to 70%, the hexagonal phase reappears. Also, by increasing the concentration of Mn^{2+} ions from 40 to 70%, the cubic phase peaks increase. Additionally, increasing the concentration of Mn^{2+} ions from 40 to 70% leads to an increase in cubic phase peaks, which is consistent with the TEM images. The zoomed image (Fig. 3b) shows that with an increase in the concentration of Mn^{2+} ions, the diffraction peak (111) slightly shifts to the lower angle side due to the substitution of Y^{3+} ions by smaller Mn^{2+} ions in the host lattice³⁶. Figure 3c displays the XRD patterns of NaYF_4 UCNPs at different Yb^{3+} concentrations ($\text{NaYF}_4:40\% \text{Mn}^{2+}/1\% \text{Yb}^{3+}$ and $\text{NaYF}_4:40\% \text{Mn}^{2+}/40\% \text{Yb}^{3+}$). The XRD patterns indicate a mixed-phase NaYF_4 crystal, consistent with standard patterns of hexagonal (JCPDS: 00-016-0334) and cubic (JCPDS: 00-021-0547) phases. The results show that increasing the Yb^{3+} concentration from 1 to 40% leads to a decrease in crystallinity. Moreover, with an increase in Yb^{3+} concentration, the cubic NaYF_4 phase increases while the hexagonal phase decreases. Therefore, the $\text{NaYF}_4:40\% \text{Mn}^{2+}/1\% \text{Yb}^{3+}$ sample was chosen as the main sample.

In summary, XRD is a powerful technique that allows for the analysis of crystal structure and purity. The XRD patterns of $\text{NaYF}_4:5\% \text{Yb}^{3+}/30\% \text{Mn}^{2+}$ UCNPs, $\text{NaYF}_4:5\% \text{Yb}^{3+}/x\% \text{Mn}^{2+}$ ($x = 30, 40, 50, 60, 70$) UCNPs, and NaYF_4 UCNPs at different Yb^{3+} concentrations were analyzed, and the results indicate mixed-phase NaYF_4 crystals with standard patterns of cubic and hexagonal phases. The crystallinity and phase composition were found to be dependent on temperature and dopant concentration, which is consistent with the TEM images.

Figure 4 displays XRD patterns of NaYF_4 and NaYF_4 UCNPs at different Er^{3+} concentrations ($\text{NaYF}_4:1\% \text{Yb}^{3+}/40\% \text{Mn}^{2+}/2\% \text{Er}^{3+}$ and $\text{NaYF}_4:1\% \text{Yb}^{3+}/40\% \text{Mn}^{2+}/10\% \text{Er}^{3+}$). The XRD pattern of the UCNPs can be assigned to a mixed-phase NaYF_4 crystal with the standard pattern of hexagonal (JCPDS: 00-016-0334) and cubic (JCPDS: 00-021-0547). No significant additional diffraction peaks were detected, even when the Er^{3+} feeding content was as high as 10 mol%. The results indicate that the crystallinity decreased with increasing Er^{3+} concentration from 2 to 10%. Additionally, with an increased Er^{3+} concentration, the XRD peak intensity increases in the cubic and hexagonal phases. Consequently, the $\text{NaYF}_4:1\% \text{Yb}^{3+}/40\% \text{Mn}^{2+}/10\% \text{Er}^{3+}$ UCNP sample was chosen as the primary sample.

Determination of optimum synthesis temperature for $\text{NaYF}_4:5\% \text{Yb}^{3+}/30\% \text{Mn}^{2+}$ nanoparticles

The UCL spectra of the different synthesis temperatures (120 °C, 140 °C, 160 °C, 180 °C, 200 °C) of $\text{NaYF}_4:5\% \text{Yb}^{3+}/30\% \text{Mn}^{2+}$ nanoparticles were measured using CW 980 nm excitation. Figure 5a displays the UCL emission spectra of these nanoparticles, revealing a relatively strong emission band at 583 nm and a weaker emission band at 575 nm under 980 nm excitation, corresponding to $\text{Mn}^{2+}: {}^4\text{A}_1 ({}^4\text{G}) \rightarrow {}^6\text{A}_1 ({}^6\text{S})$ and $\text{Mn}^{2+}: {}^4\text{T}_1 ({}^4\text{G}) \rightarrow {}^6\text{A}_1 ({}^6\text{S})$ respectively, as shown in Fig. 5a. Our objective was to determine the optimal synthesis temperature for subsequent experiments, and thus, the relationship between reaction temperature and emission intensity was crucial. As depicted in Fig. 5a, the emission intensity increased as the synthesis temperature increased from 120 to 140 °C, but significantly decreased as the synthesis temperature increased to 200 °C. Figure 5b illustrates the log intensity different synthesis temperatures (120 °C, 140 °C, 160 °C, 180 °C, 200 °C) nanoparticles, indicating that the synthesis temperature of 140 °C resulted in the highest emission intensity among all samples, which was

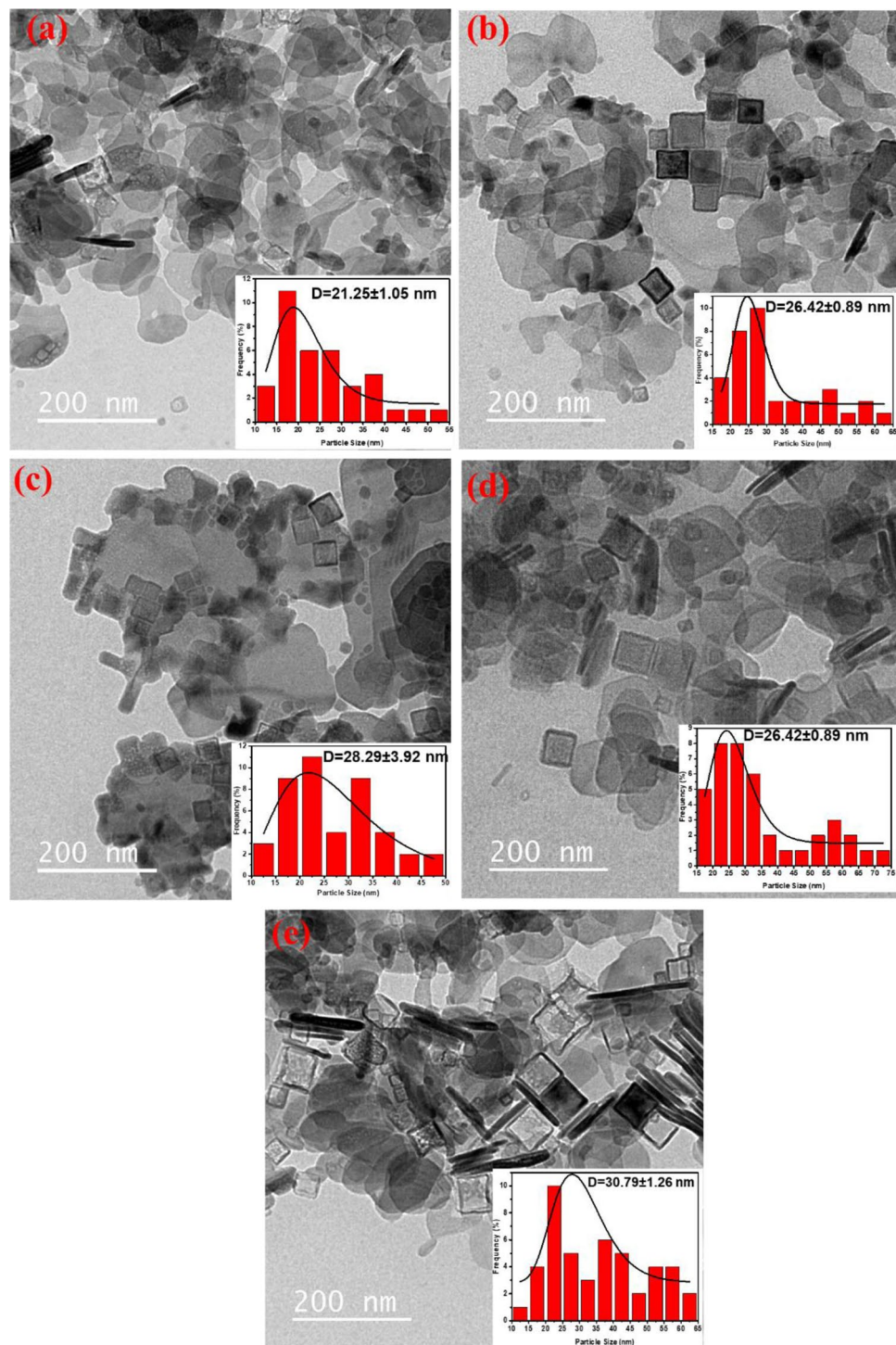


Figure 2. TEM images of NaYF₄: Mn²⁺, Yb³⁺ nanocrystals doped with (a) 30%, (b) 40%, (c) 50%, (d) 60% and (e) 70% Mn²⁺ ions. The analyzed samples were in solution form.

considered the optimum synthesis temperature. These observations were attributed to the shrinking host lattice and the decreased non-radiative relaxation processes, consistent with a previous study³⁸.

Optical properties of NaYF₄: Yb³⁺/Mn²⁺ under 980 nm excitation

Figure 5c and e present the UCL yellow emission spectra of NaYF₄: Yb³⁺/Mn²⁺ nanoparticles at their optimum synthesis temperature (140 °C). The UCL spectra were measured using CW 980 nm excitation, revealing a visible area to yellow UCL emission. The pulse duration for the impact mode was 3 min, the power density of the 980 nm laser was 1 W/cm², and the spot width was 3 mm. 1000 µl of the solution was poured into the cuvette and the

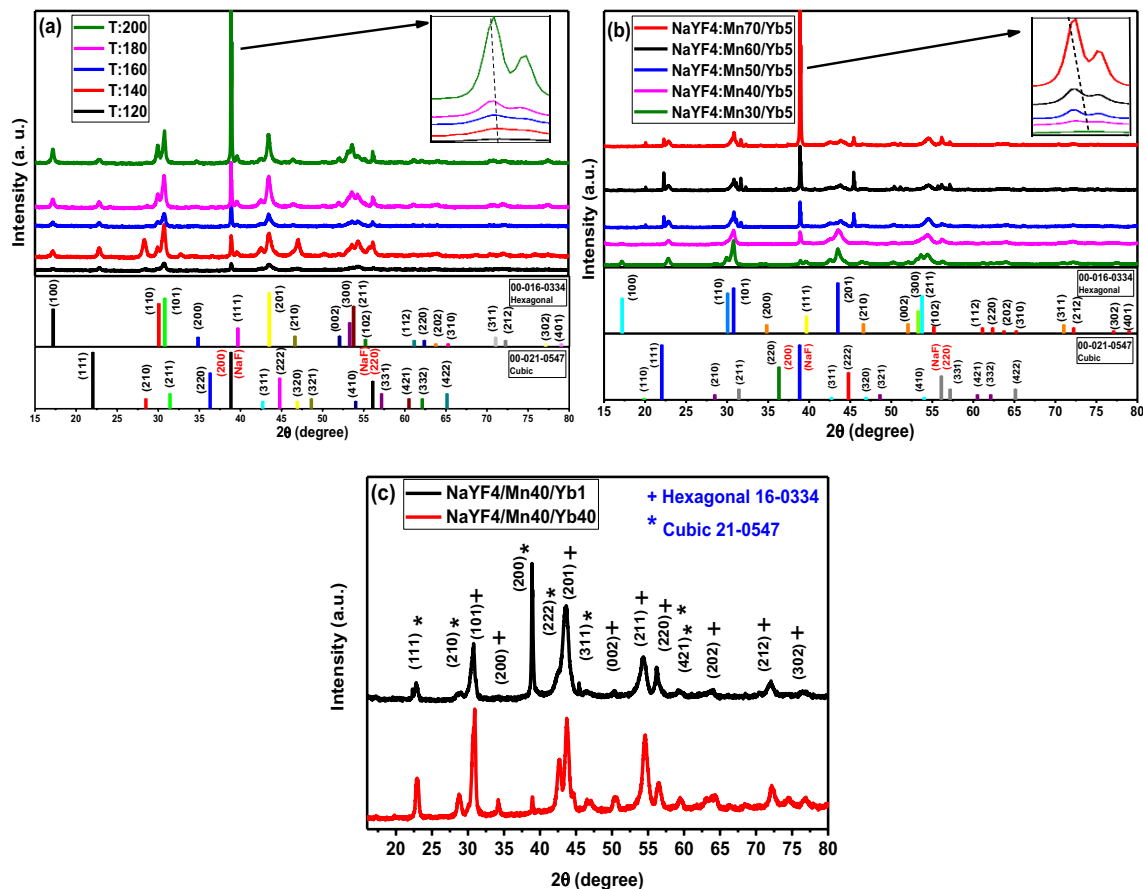


Figure 3. XRD patterns of (a) NaYF₄: 5%Yb³⁺/30%Mn²⁺ UCNPs at different synthesis temperatures (120 °C, 140 °C, 160 °C, 180 °C, 200 °C), (b) NaYF₄: 5%Yb³⁺/x%Mn²⁺ (x=30, 40, 50, 60, 70%) UCNPs, (c) NaYF₄ UCNPs at different Yb³⁺ concentration (NaYF₄:40%Mn²⁺/1%Yb³⁺ and NaYF₄:40%Mn²⁺/40%Yb³⁺). The analyzed samples were in solution form.

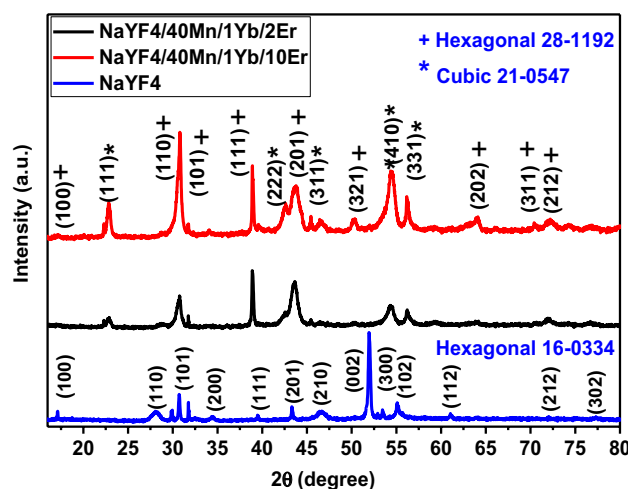


Figure 4. XRD patterns of NaYF₄, NaYF₄:1%Yb³⁺/40%Mn²⁺/2%Er³⁺ and NaYF₄:1%Yb³⁺/40%Mn²⁺/10% Er³⁺ UCNPs. The analyzed samples were in solution form.

cuvette was placed inside the measuring device. The UCL spectrum consisted of a weak emission peak at 487 nm, corresponding to the d-d transition [Mn²⁺: ⁴A₁ (⁴G) → ⁶A₁ (⁶S)] and a broadband emission peak at approximately 590 nm, corresponding to Mn²⁺: ⁴T₁ (⁴G) → ⁶A₁ (⁶S). Figure 5c illustrates the concentration-dependent UCL emission of NaYF₄: 5Yb³⁺/x%Mn²⁺ (x=20, 30, 40, 50, 60 and 70), with the optimal doping concentration of Mn²⁺ determined to be x=40%. Figure 5d displays the log intensity versus Mn²⁺ concentration, indicating an

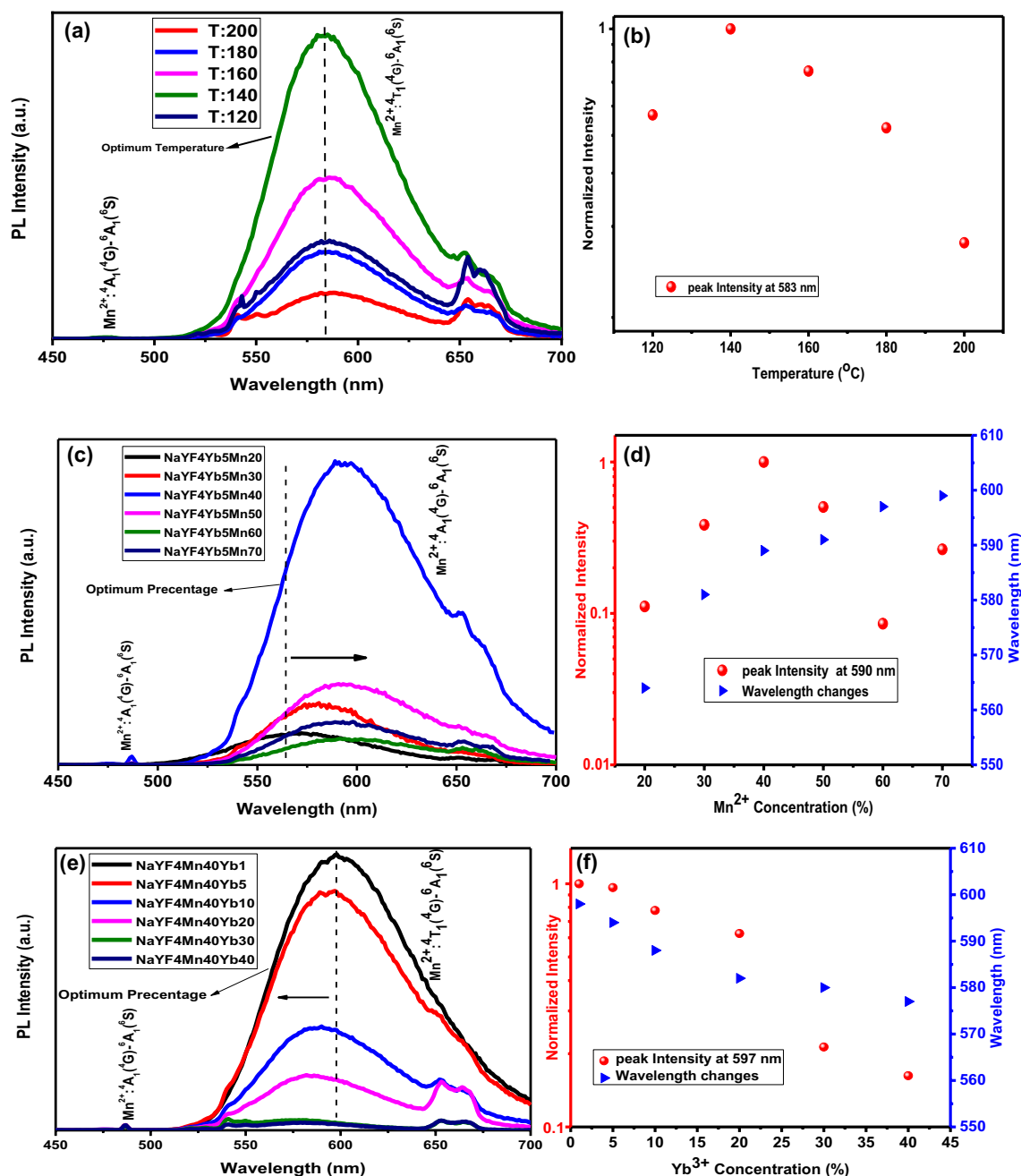


Figure 5. (a) UCL emission spectra of NaYF₄:5%Yb³⁺/30%Mn²⁺ nanoparticles with different synthesis temperatures (120 °C, 140 °C, 160 °C, 180 °C and 200 °C) and (b) log intensity versus synthesis temperature under 980 nm CW excitation. (c) UCL emission spectra of NaYF₄:5%Yb³⁺/x%Mn²⁺ (x = 20, 30, 40, 50, 60 and 70%) nanoparticles and (d) log intensity versus Mn²⁺ concentration under 980 nm CW excitation. (e) UCL emission spectra of NaYF₄:40% Mn²⁺/x%Yb³⁺ (x = 1, 5, 10, 20, 30 and 40%) nanoparticles and (f) log intensity versus Yb³⁺ concentration under 980 nm CW excitation. The pulse duration for the impact mode was 3 min, the power density of the 980 nm laser was 1 W/cm², and the spot width was 3 mm. 1000 μl of the solution was poured into the cuvette and the cuvette was placed inside the measuring device.

increase in emission intensity as the Mn²⁺ percentage increased from 20 to 40%, followed by a sharp decrease as the Mn²⁺ percentage increased to 70%. The gradual decrease in peak intensity with increasing Mn²⁺ concentration was attributed to energy transfer from Mn²⁺ to Yb³⁺³⁹. Additionally, with increasing Mn²⁺ concentration, the peak position shifted from 563 nm (yellow) to 593 nm (orange), confirming this energy transfer. Figure 5e shows the PL intensity versus Yb³⁺ concentration, indicating a decrease in emission intensity as the Yb³⁺ percentage increased from 1 to 40%, with the optimal doping concentration of Yb³⁺ determined to be x = 1³³. The decrease in peak intensity with increasing Yb³⁺ concentration was attributed to an energy transfer from Yb³⁺ to Mn²⁺³⁹. Furthermore, with increasing Yb³⁺ concentration, the peak position shifted from 599 nm (orange) to 573 nm (yellow), confirming this energy transfer (Fig. 5f). Visible photons from the excited Yb³⁺-Mn²⁺ pairs were

released via the sequential ground-state absorption (GSA, $|^2F_{7/2}, ^6A_1(^6S)\rangle \rightarrow |^2F_{5/2}, ^6A_1(^6S)\rangle$) and excited-state absorption (ESA, $|^2F_{5/2}, ^6A_1(^6S)\rangle \rightarrow |^2F_{7/2}, ^4T_1(^6S)\rangle$) processes.

Luminescence decay time of NaYF₄:Yb³⁺/Mn²⁺ nanoparticles under 980 nm excitation

To provide further evidence for the role that temperature plays in enhancing UC emission, decay curves of the UCNP are presented in Fig. 6a–f. Decay curves were fitted with the following formula proposed by Nakazawa⁴⁰:

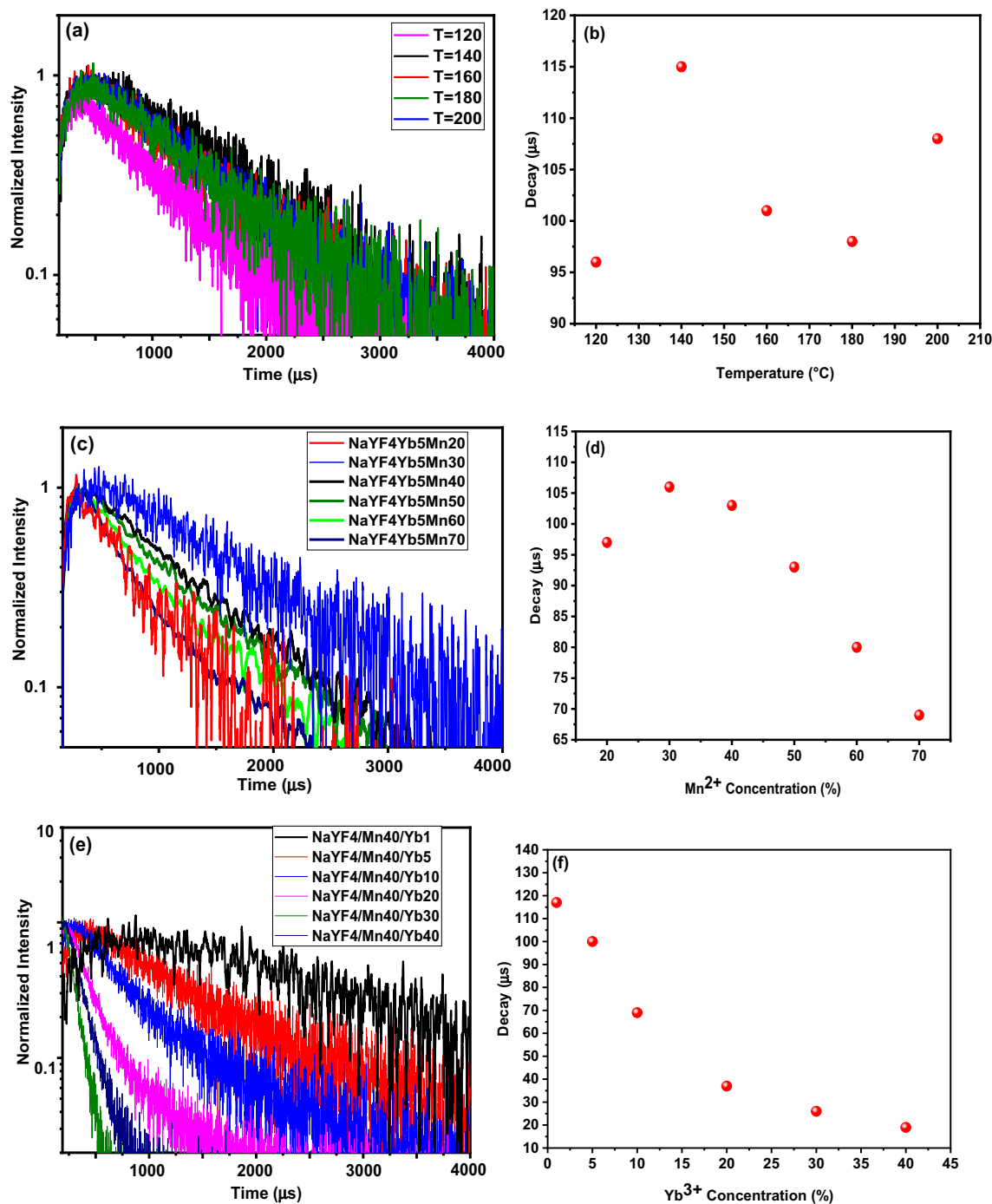


Figure 6. (a) Lifetimes spectra of NaYF₄:5%Yb³⁺/30%Mn²⁺ nanoparticles with different synthesis temperatures (120 °C, 140 °C, 160 °C, 180 °C and 200 °C) and (b) amount of decay under 980 nm pulsed excitation. (c) Lifetimes spectra of NaYF₄:5%Yb³⁺/x%Mn²⁺ (x%=20,30,40,50,60 and 70) nanoparticles, (d) amount of decay under 980 nm pulsed excitation. (e) Lifetimes spectra of NaYF₄:40% Mn²⁺/x%Yb³⁺ (x%=1,5,10,20,30 and 40) nanoparticles, (f) amount of decay under 980 nm pulsed excitation. The power density and spot diameter of the used 980-nm laser are 10 W/cm² and 3.0 mm, respectively. Luminescence decay times were measured in the red wavelength region. The analyzed samples were in solution form.

$$\tau_m = \frac{\int_0^{\infty} I(t) dt}{\int_0^{\infty} I(t) dt}$$

where τ_m is the effective decay time constant, and $I(t)$ is the intensity at time t .

Figure 6 displays the UC luminescence decay curves of (a) NaYF₄:5%Yb³⁺/30%Mn²⁺ nanoparticles at different synthesis temperatures (120 °C, 140 °C, 160 °C, 180 °C and 200 °C), (b) the amount of decay under 980 nm pulsed excitation, (c) NaYF₄:5%Yb³⁺/x% Mn²⁺ (x% = 20, 30, 40, 50, 60 and 70) nanoparticles decay, (d) the amount of decay under 980 nm pulsed excitation, (e) NaYF₄:40% Mn²⁺/x%Yb³⁺ (x% = 1, 5, 10, 20, 30 and 40) nanoparticles decay, and (f) the amount of decay under 980 nm pulsed excitation. The pulse duration for the impact mode was 3 min, the power density of the 980 nm laser was 10 W/cm², and the spot width was 3 mm. 1000 μ l of the solution was poured into the cuvette and the cuvette was placed inside the measuring device.

Figures 6a and b show that the luminescence lifetimes increase from 96 to 115 μ s as the synthesis temperature rises from 120 to 140 °C, while as the synthesis temperature increases from 140 to 200 °C, the luminescence lifetimes decrease. Therefore, the NaYF₄:5%Yb³⁺/30%Mn²⁺ nanoparticles with a synthesis temperature of 140 °C, showing the longest luminescence lifetime, were selected as the main sample. As previously demonstrated, a synthesis temperature of 140 °C is the optimal synthesis temperature for producing samples. Figure 6c and d reveal that by increasing the Mn²⁺ concentration from 20 to 70%, the luminescence lifetimes of the Yb³⁺: ²F_{5/2} level first increase and then decrease significantly. The luminescence lifetimes for Yb³⁺ were found to decrease monotonically with increasing Mn²⁺ concentration, providing evidence for efficient energy transfer from Yb³⁺ to Mn²⁺ ions³⁷. These time-decay measurements are consistent with the UCL emission spectra. Figure 6e and f illustrate that by increasing Yb³⁺ concentration from 1 to 40%, the luminescence lifetimes of the Yb³⁺: ²F_{5/2} level decrease significantly from 116 to 15 μ s. The luminescence lifetimes for NaYF₄: 40%Mn²⁺/x%Yb³⁺ (x% = 1, 5, 10, 20, 30 and 40) UCNP were found to decrease monotonically with increasing Yb³⁺ concentration, providing evidence for efficient energy transfer from Yb³⁺ to Mn²⁺ ions³⁷. Our main objective was to find a combination of Yb³⁺ and Mn²⁺ that had the longest luminescence lifetime. Therefore, a sample of NaYF₄: 40%Mn²⁺/1% Yb³⁺ was selected as the main sample and used in the subsequent steps. These results are in good agreement with the UCL emission spectra and observed structural properties.

Optical properties of NaYF₄:Er³⁺/Mn²⁺ nanoparticles under 980 nm excitation

To investigate the energy transfer between Mn²⁺ and Er³⁺ and the luminescence properties of NaYF₄: Er³⁺/Mn²⁺, the UCL emission spectra of synthetic samples were measured under CW 980 nm excitation. The pulse duration for the impact mode was 3 min, the power density of the 980 nm laser was 1 W/cm², and the spot width was 3 mm. 1000 μ l of the solution was poured into the cuvette and the cuvette was placed inside the measuring device. Figure 7a displays the UCL emission spectra of NaYF₄: 5%Er³⁺/x%Mn²⁺ (x% = 20, 30, 40, 50, 60 and 70) nanoparticles. The UCL spectra consist of four emission bands centered at 486 nm (blue), 524 nm (green), 549 nm (green), and 654 nm (red), corresponding to the transitions of ⁴A₁ (⁴G) → ⁶A₁ (⁶S), ²H_{11/2} → ⁴I_{15/2}, ²S_{3/2} → ⁴I_{15/2} and ²F_{9/2} → ⁴I_{15/2}, respectively. The UCL spectra in Fig. 7a demonstrate that the green and blue emissions increase when the Mn²⁺ concentration increases to 40%, but then decrease when it increases to 70%. Additionally, the red emission decreases when the Mn²⁺ concentration increases from 20 to 70%⁴¹. These results suggest that increasing the Mn²⁺ concentration leads to a continuous decrease in the emission intensity of Er³⁺, indicating the possibility of energy transfer from Er³⁺ ions to Mn²⁺⁴².

To gain further insight into the mechanism of Mn²⁺ doped NaYF₄: 2%Er³⁺ nanoparticles, the log intensity versus Mn²⁺ concentration for 524 nm, 549 nm, and 654 nm was calculated and presented in Fig. 7b. The green emission intensity increases as the Mn²⁺ concentration increases from 20 to 40%, but then decreases as it increases to 70%. Moreover, the red emission intensity decreases as the Mn²⁺ concentration increases from 20 to 70%, confirming the role of Mn²⁺ in enhancing the green and blue emission and suppressing the red emission in the NaYF₄: Er³⁺/Mn²⁺ system⁴¹.

Figure 7c shows the UCL emission spectra of the NaYF₄: 40Mn²⁺/x%Er³⁺ (x% = 1, 2, 5 and 10) nanoparticles. The spectra consist of four emission bands centered at 486 nm (blue), 524 nm (green), 549 nm (green), and 654 nm (red), corresponding to the transitions of ⁴A₁ (⁴G) → ⁶A₁ (⁶S), ²H_{11/2} → ⁴I_{15/2}, ²S_{3/2} → ⁴I_{15/2} and ²F_{9/2} → ⁴I_{15/2}, respectively. The results indicate that as the Er³⁺ concentration increases from 1 to 10%, the green and blue emissions decrease, while the red emission increases⁴¹. This finding suggests that increasing the Er³⁺ concentration leads to a continuous decrease in the emission intensity of Mn²⁺, indicating the possibility of energy transfer from Mn²⁺ ions to Er³⁺⁴².

To gain a deeper understanding of the mechanism of Er³⁺ doped NaYF₄: 40%Mn²⁺ nanoparticles, the log intensity versus Er³⁺ concentration for 524 nm, 549 nm, and 654 nm was calculated and presented in Fig. 7d. The results show that as the Er³⁺ concentration increases from 1 to 10%, the green UC emission bands at 524 nm (Er³⁺: ²H_{11/2} → ⁴I_{15/2}) and 549 nm (Er³⁺: ⁴S_{3/2} → ⁴I_{15/2}) and blue UC emission bands at 486 nm (Mn²⁺: ⁴A₁ (⁴G) → ⁶A₁) decrease, while the red UC emission bands at 654 nm (Er³⁺: ²F_{9/2} → ⁴I_{15/2}) increase, confirming the role of Er³⁺ in reducing the green and blue emission and enhancing the red emission in NaYF₄: Er³⁺/Mn²⁺ systems⁴¹. First of all, the possible energy transfer from Er³⁺ to Mn²⁺-Yb³⁺ dimer, which contributes to the emission intensity as 524 and 549 nm decreased, can be explained by the following mechanisms: ⁴S_{3/2} (Er³⁺) ²F_{7/2}, ⁶A₁ (Mn²⁺-Yb³⁺ dimer) ⁴I_{15/2} (Er³⁺) ²F_{7/2}, ⁴T₁ (Mn²⁺-Yb³⁺ dimer). Secondly, the increased luminescent centers lead the emission intensity at 657 nm (Er³⁺: ⁴F_{9/2} → ⁴I_{15/2}) may be energy transfer from Mn²⁺-Yb³⁺ dimer to Er³⁺ ions. The mechanism of energy transfer from Mn²⁺-Yb³⁺ dimer to Er³⁺ ions was proposed as follows: |²F_{7/2}, ⁴T₁) (Mn²⁺-Yb³⁺ dimer) + ⁴I_{15/2} (Er³⁺) → ⁴F_{9/2} (Er³⁺) + |²F_{7/2}, ⁶A₁) (Mn²⁺-Yb³⁺ dimer), so the energy transfer bridge was constituted by the energy transfer process between Er³⁺ ion and the Mn²⁺-Yb³⁺ dimer.

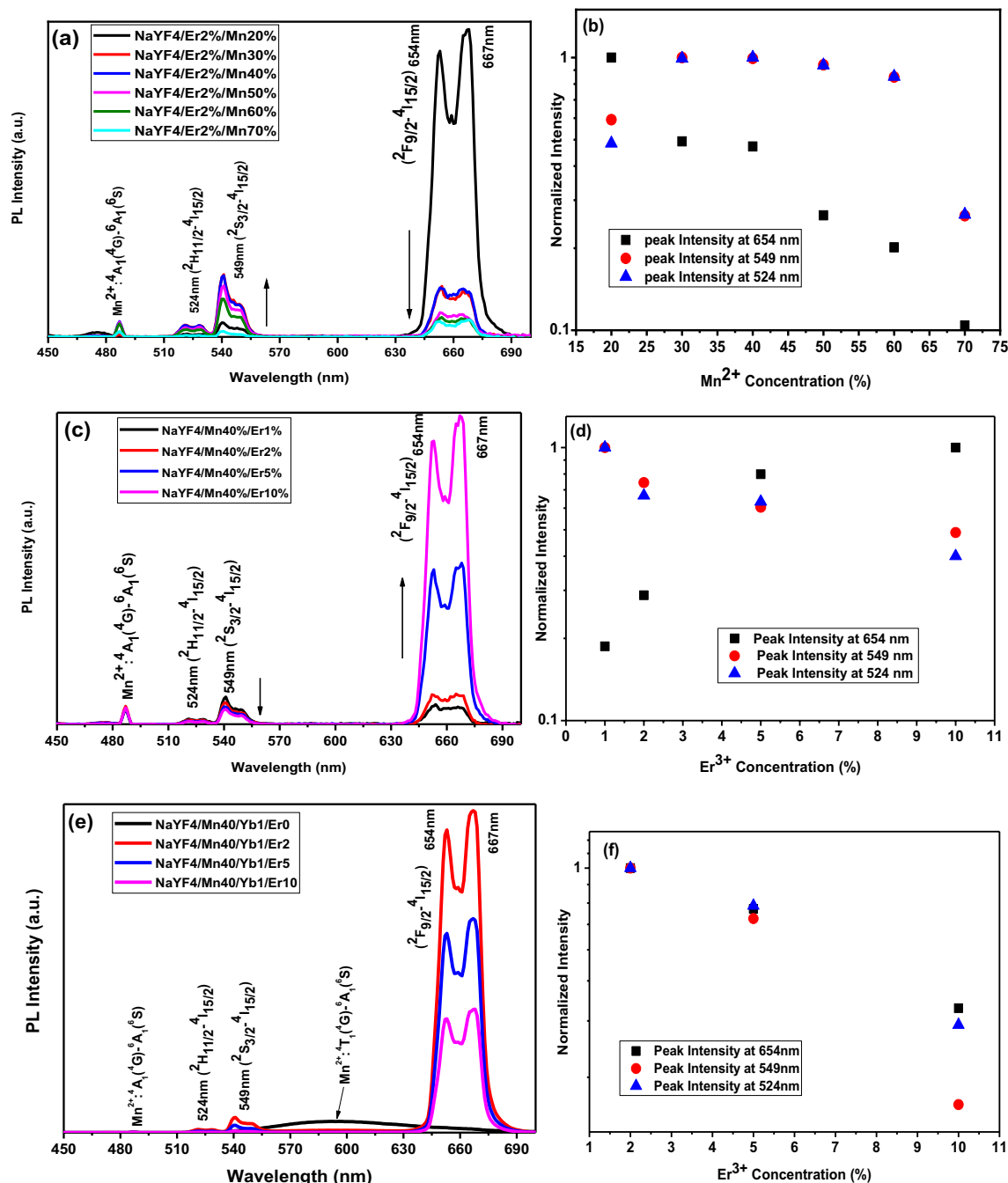


Figure 7. (a) UCL emission spectra of NaYF₄: 40% Mn²⁺/x%Er³⁺ (x = 1, 2, 5 and 10) nanoparticles and (b) log intensity versus Er³⁺ concentration under 980 nm CW excitation. (c) UCL emission spectra of NaYF₄: 2% Er³⁺/x%Mn²⁺ (x = 20, 30, 40, 50, 60 and 70) nanoparticles (d) log intensity versus Mn²⁺ concentration under 980 nm CW excitation. (e) UCL emission spectra of NaYF₄: 1% Yb³⁺/40% Mn²⁺/x%Er³⁺ (x = 0, 2, 5, and 10) nanoparticles (f) log intensity versus Er³⁺ concentration under 980 nm CW excitation. NaYF₄:Yb³⁺/Mn²⁺ nanoparticles emitted relatively strong emission band at 575 nm. The pulse duration for the impact mode was 3 min, the power density of the 980 nm laser was 1 W/cm², and the spot width was 3 mm. 1000 μ l of the solution was poured into the cuvette and the cuvette was placed inside the measuring device.

To further investigate the impact of Er³⁺ doping on the upconversion luminescence (UCL) properties of Yb³⁺/Er³⁺/Mn²⁺ triply-doped NaYF₄ nanoparticles, the emission intensity versus wavelength of NaYF₄: 1%Yb³⁺/40%Mn²⁺/x%Er³⁺ (x = 0, 2, 5, and 10) nanoparticles at the optimum synthesis temperature is presented in Fig. 7e. When excited at 980 nm, five UCL bands at 486 nm, 524 nm, 549 nm, 595 nm, and 654 nm are detected, which are attributed to the ⁴A₁(⁴G) → ⁶A₁(⁶S), ²H_{11/2} → ⁴I_{15/2}, ²S_{3/2} → ⁴I_{15/2}, ⁴T₁(⁴G) → ⁶A₁(⁶S) and ²F_{9/2} → ⁴I_{15/2} transitions, respectively. The results show that as the Er³⁺ concentration increases from 0 to 10%, all emission bands, blue, orange, and green, disappear for the NaYF₄:Mn²⁺/Yb³⁺/Er³⁺ nanoparticles. This single-band

UCL emission can be attributed to a non-radiative energy transfer from the $^4S_{3/2}$ and $^2H_{11/2}$ levels of Er^{3+} to the 4T_1 and 4A_1 levels of Mn^{2+} ⁴³. The disappearance of green emissions with increasing Er^{3+} concentration suggests an efficient exchange energy transfer process between Mn^{2+} and Er^{3+} ions, which is attributed to their proximity and nearly perfect overlap of energy levels in the host lattices^{33,44–46}. Additionally, it is noteworthy that the red emission intensity gradually decreases with the increase in Er^{3+} concentration due to concentration quenching between neighboring Er^{3+} ions⁴³.

In Fig. 7c, the luminescence of sample $NaYF_4: 10\%Er^{3+}, 40\%Mn^{2+}$ is the highest. But when the three dopants, namely; manganese, yttrium and ytterbium are added to $NaYF_4$, sample $NaYF_4: 1\%Yb^{3+}/40\%Mn^{2+}/2\%Er^{3+}$ is the highest, so we consider sample $NaYF_4: 1\%Yb^{3+}/40\%Mn^{2+}/2\%Er^{3+}$ as the optimal sample (Fig. 7e).

To better comprehend the UCL mechanism, the log intensity versus Er^{3+} concentration for $NaYF_4: 1\%Yb^{3+}/40\%Mn^{2+}/x\%Er^{3+}$ ($x=0, 2, 5, 10$) nanoparticles under CW 980 nm excitation is calculated and presented in Fig. 7f. The results show that as the Er^{3+} concentration increases, the green emission disappears and the red emission intensity decreases.

To further investigate the effect of Mn^{2+} on the upconversion luminescence (UCL) properties of $Yb^{3+}/Mn^{2+}/Er^{3+}$ triply-doped $NaYF_4$ nanoparticles, a diagram of energy levels and corresponding energy transfer mechanisms is presented in Fig. 8a. When Mn^{2+} ions are introduced into $NaYF_4: Yb^{3+}/Er^{3+}$, a new energy transfer process between Er^{3+} and Mn^{2+} is induced under the excitation of 980 nm CW laser. This process leads to a decrease in the radiative transition rate of $Er^{3+}:H_{11/2}$ and $Er^{3+}:S_{3/2}$ levels to the ground state, while the population density of $Mn^{2+}:^4T_1$ increases due to the resonance energy transfer. Subsequently, a back-energy transfer from 4T_1 of Mn^{2+} to the $^4F_{7/2}$ level of Er^{3+} leads to an enhancement in the red emission. Here, the direct multi-phonon relaxation process and the indirect energy transfer process of ($F_{5/2}(Yb^{3+}), ^4I_{13/2}(Er^{3+}) \rightarrow ^2F_{7/2}(Yb^{3+}), ^7I_{9/2}(Er^{3+})$) are expected to have a minor contribution to the population of $^4S_{3/2}$ energy level in Er^{3+} ions. It is noteworthy that the $Er^{3+}:F_{9/2}$ lifetime is shorter than that of $Mn^{2+}:^4T_1$, which explains why no orange luminescence is observed corresponding to the $Mn^{2+}:^4T_1 \rightarrow ^6A_1$ transition. A similar mechanism has been discussed in $NaYF_4$ by Zhangyu Huang et al.³⁴. The schematic of energy level diagrams of $Mn^{2+}-Yb^{3+}$ dimer is shown in Fig. 8b. For the $Mn^{2+}-Yb^{3+}$ dimer, the sensitization through the $Mn^{2+}-Yb^{3+}$ dimer complex entails both ground state absorption (GSA) and excited state absorption (ESA). The $Mn^{2+}-Yb^{3+}$ dimer ground state is represented by $|^2F_{7/2}, ^6A_1\rangle$, the intermediate excited state in the NIR by $|^2F_{5/2}, ^6A_1\rangle$, and the relevant higher excited states by $|^2F_{7/2}, ^4T_1\rangle$ and $|^2F_{7/2}, ^4T_2\rangle$.

Luminescence decay time of $NaYF_4: 1\%Yb^{3+}/40\%Mn^{2+}/x\%Er^{3+}$ ($x=0, 2, 5, \text{ and } 10$) nanoparticles under 980 nm excitation

To provide further evidence of the role played by Er^{3+} in enhancing UC emission, Fig. 9a and b presents the decay curves of the UCNPs. The pulse duration for the impact mode was 3 min, the power density of the 980 nm laser was 10 W/cm², and the spot width was 3 mm. 1000 μ l of the solution was poured into the cuvette and the cuvette was placed inside the measuring device. Figure 9a shows the lifetime spectra of $NaYF_4: 1\%Yb^{3+}/40\%Mn^{2+}/x\%Er^{3+}$ ($x=0, 2, 5, \text{ and } 10$) nanoparticles, while Fig. 9b shows the amount of decay under 980 nm pulsed excitation. The luminescence lifetimes of $NaYF_4: Yb^{3+}/Mn^{2+}/Er^{3+}$ were found to decrease monotonically with increasing Er^{3+} concentration. This provides evidence for efficient energy transfer from Yb^{3+} to Mn^{2+} ions³⁸. The decrease in lifetime is likely due to a competitive effect between the energy transfer of Er^{3+} and Mn^{2+} ions and the decrease in radiative transition probability resulting from increased local symmetry after Er^{3+} doping. The former prolongs the lifetime, while the latter decreases it.

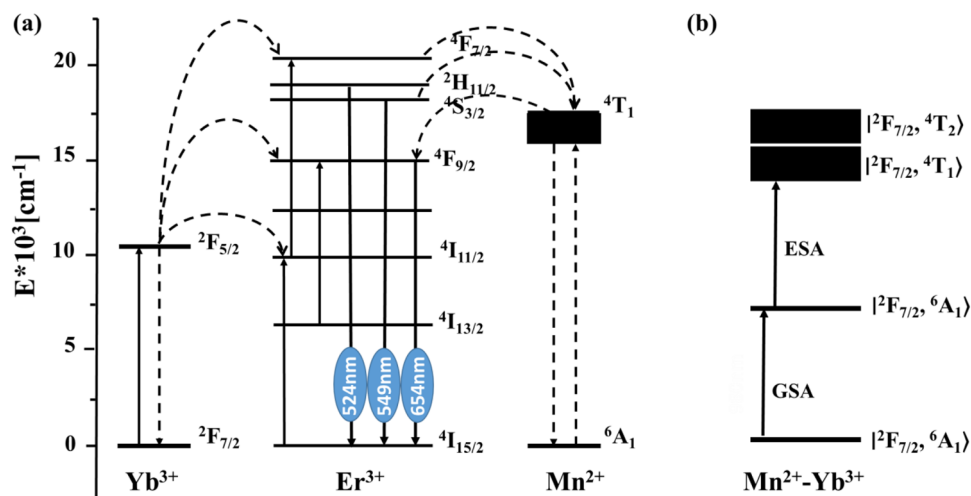


Figure 8. (a) Schematic of energy level diagrams of $NaYF_4:Yb^{3+}/Mn^{2+}/Er^{3+}$ and the proposed mechanism of the UC process under the excitation of 980 nm. (b) Schematic of energy level diagrams of $Mn^{2+}-Yb^{3+}$ dimer.

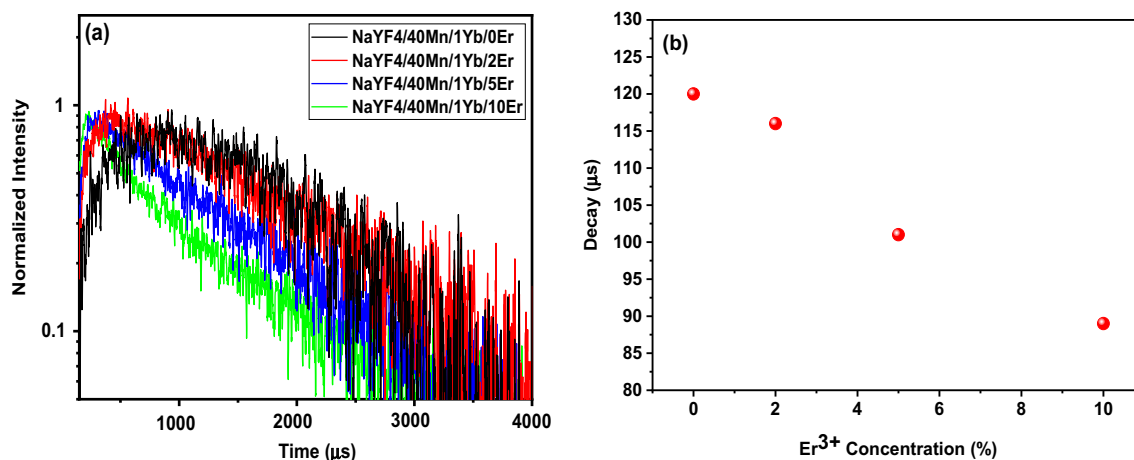


Figure 9. (a) Lifetimes spectra of NaYF₄: 1% Yb³⁺/40% Mn²⁺/x%Er³⁺ (x = 0, 2, 5, and 10) nanoparticles, (b) amount of decay under 980 nm pulsed excitation. The power density and spot diameter of the used 980-nm laser are 10 W/cm² and 3.0 mm, respectively. Luminescence decay times were measured in the red wavelength region. The analyzed samples were in solution form.

Conclusions

In this study, we investigated the UC energy transfer mechanism of Yb³⁺/Mn²⁺/Er³⁺ tri-doped uniform cubic NaYF₄ nanoparticles under 980 nm excitation in pulsed or continuous-wave modes. Firstly, we synthesized NaYF₄:5%Yb³⁺/30%Mn²⁺ nanoparticles at different synthesis temperatures, and the optimal synthesis temperature of 140 °C was selected for subsequent experiments. Next, we studied NaYF₄:5%Yb³⁺ nanoparticles with varying x%Mn²⁺ (x = 20, 30, 40, 50, 60, 70) concentration and NaYF₄:40% Mn²⁺ nanoparticles with varying x%Yb³⁺ (x = 1, 5, 10, 20, 30, 40) concentration. Finally, we synthesized NaYF₄:40% Mn²⁺/1%Yb³⁺ nanoparticles with different x%Er³⁺ (x = 0, 2, 5, 10) concentrations by selecting the optimal Mn²⁺ and Yb³⁺ concentrations. The UCL spectra of NaYF₄: 1% Yb³⁺/40% Mn²⁺/x%Er³⁺ (x = 0, 2, 5, and 10) nanoparticles exhibited four emission bands centered at 486 nm (blue), 524 nm (green), 549 nm (green), and 654 nm (red), corresponding to the transitions of ⁴A₁ (4G) → ⁶A₁ (⁶S), ²H_{11/2} → ⁴I_{15/2}, ²S_{3/2} → ⁴I_{15/2}, and ²F_{9/2} → ⁴I_{15/2}, respectively. As the concentration of Er³⁺ increased from 1 to 10 mol%, the green and blue emission intensities decreased, while the red emission intensity increased. This confirms the role of Er³⁺ in enhancing green and blue emission and suppressing red emission in NaYF₄:Er³⁺/Mn²⁺ systems. These findings introduce the application of Mn²⁺ in Yb³⁺-Er³⁺ codoped NaYF₄ UCNPs in color modulation, temperature sensing, and optical heating. The data presented in this study may provide useful information for further development of Ln-doped nanoparticles for these applications.

Data availability

The datasets used and analyzed during the current study available from the corresponding author on reasonable request.

Received: 25 May 2023; Accepted: 13 October 2023

Published online: 16 October 2023

References

- Bloembergen, N. Solid state infrared quantum counters. *Phys. Rev. Lett.* **2**, 84–85 (1959).
- Auzel, F. Compteur quantique par transfert d'énergie entre deux ions de terres rares dans un tungstate mixte et dans un verre. *CR Acad. Sci. Paris* **262**, 1016–1019 (1966).
- Van Uitert, L. G. & Johnson, L. F. Energy transfer between rare-earth ions. *J. Chem. Phys.* **44**, 3514–3522 (1966).
- Heer, S., Kompe, K., Gudel, H. U. & Haase, M. Highly efficient multicolour upconversion emission in transparent colloids of lanthanide-doped NaYF₄ nanocrystals. *Adv. Mater.* **16**, 2102–2105 (2004).
- Suyver, J. F. *et al.* Novel materials doped with trivalent lanthanides and transition metal ions showing near-infrared to visible photon upconversion. *Opt. Mater.* **27**, 1111–1130 (2005).
- Haase, M. & Schafer, H. Upconverting nanoparticles. *Angew. Chem Int. Ed.* **50**, 5808–5829 (2011).
- Shan, J. & Ju, Y. A single-step synthesis and the kinetic mechanism for monodisperse and hexagonal-phase NaYF₄: Yb, Er upconversion nanophosphors. *Nanotechnology* **20**, 11969 (2009).
- Dou, Q. Q., Idris, N. M. & Zhang, Y. Sandwich-structured upconversion nanoparticles with tunable color for multiplexed cell labeling. *Biomaterials*. **34**, 1722–1731 (2013).
- Wang, F. *et al.* Simultaneous phase and size control of upconversion nanocrystals through lanthanide doping. *Nature* **463**, 1061–1065 (2010).
- Priyam, A., Idris, N. M. & Zhang, Y. Gold nanoshell coated NaYF₄ nanoparticles for simultaneously enhanced upconversion fluorescence and darkfield imaging. *J. Mater. Chem.* **22**, 960–965 (2012).
- He, E. *et al.* Enhancement and regulation of fluorescence emission from NaYF₄: Yb³⁺, Er³⁺ nanocrystals by codoping Mn²⁺ ions. *J. Nanosci. Nanotechnol.* **14**, 4139–4146 (2014).
- Auzel, F. Upconversion and anti-stokes processes with f and d ions in solids. *Chem. Rev.* **104**, 139–173 (2004).
- Li, Z. Q. & Zhang, Y. Facile synthesis of lanthanide nanoparticles with paramagnetic, down-and up-conversion properties. *Nanoscale* **2**, 1240–1243 (2010).
- Liu, H. *et al.* Photon upconversion kinetic nanosystems and their optical response. *Laser Photon. Rev.* **12**, 1700144 (2017).

15. He, J. *et al.* Plasmonic enhancement and polarization dependence of nonlinear upconversion emissions from single gold nanorod@SiO₂@CaF₂:Yb³⁺, Er³⁺ hybrid core-shell-satellite nanostructures. *Light Sci. Appl.* **6**, 16217–16217 (2017).
16. Yu, X. F. *et al.* Victims and vectors: Highly pathogenic avian influenza H5N1 and the ecology of wild birds. *Nano Res.* **3**, 51–73 (2010).
17. Zhang, Q. & Zhang, Q. M. Synthesis and photoluminescent properties of α -NaYF₄: Nd/ α -NaYF₄ core/shell nanostructure with enhanced near infrared (NIR) emission. *Mater. Lett.* **63**, 376–378 (2009).
18. Liu, Y., Tu, D., Zhu, H. & Chen, X. Lanthanide-doped luminescent nanoprobes: Controlled synthesis, optical spectroscopy, and bioapplications. *Chem. Soc. Rev.* **42**, 6924–6958 (2013).
19. Wang, L., Li, Y., Zhang, Y., Gu, H. & Chen, W. Rare earth compound nanowires: Synthesis, properties and applications. *Rev. Nanosci. Nanotech.* **3**, 1–19 (2014).
20. Wang, X. *et al.* Influence of doping and excitation powers on optical thermometry in Yb³⁺-Er³⁺ doped CaWO₄. *Sci. Rep.* **7**, 1–9 (2017).
21. Rakov, N. & Maciel, G. S. Three-photon upconversion and optical thermometry characterization of Er³⁺: Yb³⁺ co-doped yttrium silicate powders. *Sens. Actuator. B* **164**, 96–100 (2012).
22. Wang, X. *et al.* Excitation powder dependent optical temperature behavior of Er³⁺ doped transparent Sr_{0.69}La_{0.31}F_{2.31} glass ceramics. *Opt. Express.* **24**, 17792–17804 (2016).
23. Xu, W., Zhao, H., Zhang, Z. & Cao, W. highly sensitive optical thermometry through thermally enhanced near infrared emissions from Nd³⁺/Yb³⁺ codoped oxyfluoride glass ceramic. *Sens. Actuator. B* **178**, 520–524 (2013).
24. Li, L., Guo, C., Jiang, S., Agrawal, D. K. & Li, T. Green up-conversion luminescence of Yb³⁺-Er³⁺ co-doped CaLa₂ZnO₅ for optically temperature sensing. *RSC Adv.* **4**, 6391–6396 (2014).
25. Wang, X. *et al.* Optical temperature sensing of rare-earth ion doped phosphors. *RSC Adv.* **5**, 86219–86236 (2015).
26. Min, Q. *et al.* Temperature sensing based on the up-conversion emission of Tm³⁺ in a single KLuF₄ microcrystal. *J. Alloys Compd.* **728**, 1037–1042 (2017).
27. Qiang, Q. & Wang, Y. Enhanced optical temperature sensing and upconversion emissions based on the Mn²⁺ codoped NaGdF₄: Yb³⁺, Ho³⁺ nanophosphor. *New J Chem.* **43**, 5011–5019 (2019).
28. Dan, H. K. *et al.* Effect of Mn²⁺ ions on the enhancement red upconversion emission of Mn²⁺/Er³⁺/Yb³⁺ tri-doped in transparent glass-ceramics. *Opt Laser Technol.* **64**, 264–268 (2014).
29. Tian, G. *et al.* Mn²⁺ dopant-controlled synthesis of NaYF₄: Yb/Er upconversion nanoparticles for *in vivo* imaging and drug delivery. *Adv. Mater.* **24**, 1226–1231 (2012).
30. Ye, S., Song, E. H. & Zhang, Q. Y. Transition metal-involved photon upconversion. *Adv. Sci.* **3**, 1600302 (2016).
31. Dan, H. K. *et al.* Effect of Mn²⁺ ions on the enhancement red upconversion emission of Mn²⁺/Er³⁺/Yb³⁺ tri-doped in transparent glass-ceramics. *Opt. Laser Technol.* **64**, 264–268 (2014).
32. Zeng, S. J. *et al.* Simultaneous realization of phase/size manipulation upconversion luminescence enhancement, and blood vessel imaging in multifunctional nanoprobes through transition metal Mn²⁺ doping. *Adv. Funct. Mater.* **24**, 4051–4059 (2014).
33. MacKenzie, L. E., Alvarez-Ruiz, D. & Pal, R. Low-temperature open-air synthesis of PVP-coated NaYF₄: Yb, Er, Mn upconversion nanoparticles with strong red emission. *R. Soc. Open Sci.* **9**, 211508 (2022).
34. Huang, Z., Gao, H. & Mao, Y. Understanding the effect of Mn²⁺ on Yb³⁺/Er³⁺ upconversion and obtaining a maximum upconversion fluorescence enhancement in inert-core/active-shell/inert-shell structures. *RSC Adv.* **6**, 83321–83327 (2016).
35. Gholizadeh, M., Zarei, M. R., Mohammadi, A. A., Ehsani, M. H. & Rezagholipour, D. H. "Design and fabrication of MgF₂ single-layer antireflection coating by glancing angle deposition. *Mater. Res. Inno.* **24**, 442–446 (2020).
36. Qiang, Q. & Wang, Y. Effect of Mn²⁺ on upconversion emission, thermal sensing and optical heater behavior of Yb³⁺ - Er³⁺ Codoped NaGdF₄ nanophosphors. *Front. Chem.* **7**, 425 (2019).
37. Prorok, K. *et al.* Near-infrared excited luminescence and *in vitro* imaging of HeLa cells by using Mn²⁺ enhanced Tb³⁺ and Yb³⁺ cooperative upconversion in NaYF₄ nanocrystals. *Nanoscale Adv.* **1**, 3463–3473 (2019).
38. Song, E. *et al.* Long-lived photon upconversion phosphorescence in RbCaF₃: Mn²⁺, Yb³⁺ and the dynamic color separation effect. *Iscience* **19**, 597–606 (2019).
39. Gao, G. & Wondraczek, L. Near-infrared down-conversion in Mn²⁺-Yb³⁺ co-doped Zn₂GeO₄. *J. Mater. Chem. C* **1**, 1952–1958 (2013).
40. Nakazawa, E., Shionoya, S. & Yen, W. M. *Phosphor Handbook* 102 (CRC Press, 1999).
41. Wang, R., Yuan, M., Zhang, Ch., Wang, H. & Xu, X. Tunable multicolor and enhanced red emission of monodisperse CaF₂: Yb³⁺/Ho³⁺ microspheres via Mn²⁺ doping. *Opt. Mater.* **79**, 403–407 (2018).
42. Cheng, C., Zeng, N., Jiao, Q., Zhang, X. & Liu, X. Tunable upconversion white photoemission in Yb³⁺/Mn²⁺/Tm³⁺ tri-doped transparent glass ceramics. *Opt. Mater.* **100**, 109718 (2020).
43. Bai, Z. *et al.* The single-band red upconversion luminescence from morphology and size controllable Er³⁺/Yb³⁺ doped MnF₂ nanostructures. *J. Mater. Chem. C* **2**, 1736–1741 (2014).
44. Zhang, Y., Lin, J. D., Vijayaragavan, V., Bhakoo, K. K. & Tan, T. T. Y. Tuning sub-10 nm single-phase NaMnF₃ nanocrystals as ultrasensitive hosts for pure intense fluorescence and excellent T1 magnetic resonance imaging. *Chem. Commun.* **48**, 10322–10324 (2012).
45. Szczesnak, A., Grzyb, T., Nowaczyk, G. & Eknor-Grzyb, A. Emission colour changes in the CaF₂ sub-microspheres doped with Yb³⁺, Er³⁺ and Mn²⁺ ions. *J. Alloys Compd.* **817**, 152718 (2020).
46. Yuan, M. *et al.* Revisiting the enhanced red upconversion emission from a single β -NaYF₄:Yb/Er microcrystal by doping with Mn²⁺ ions. *Nanoscale Res. Lett.* **14**, 103 (2019).

Acknowledgements

The authors thank Dr. Haichun Liu and Dr. Lucia Labrador Paez for their valuable advice.

Author contributions

R.Z.M. and H.A. wrote the main manuscript text. R.Z.M. collaborated in laboratory work. H.R.D. and M.H.E. have determined the issue. H.R.D. cooperated in choosing the topic and writing the article. All authors reviewed the manuscript.

Competing interests

The authors declare no competing interests.

Additional information

Supplementary Information The online version contains supplementary material available at <https://doi.org/10.1038/s41598-023-44947-1>.

Correspondence and requests for materials should be addressed to R.Z.M. or M.H.E.

Reprints and permissions information is available at www.nature.com/reprints.

Publisher's note Springer Nature remains neutral with regard to jurisdictional claims in published maps and institutional affiliations.



Open Access This article is licensed under a Creative Commons Attribution 4.0 International License, which permits use, sharing, adaptation, distribution and reproduction in any medium or format, as long as you give appropriate credit to the original author(s) and the source, provide a link to the Creative Commons licence, and indicate if changes were made. The images or other third party material in this article are included in the article's Creative Commons licence, unless indicated otherwise in a credit line to the material. If material is not included in the article's Creative Commons licence and your intended use is not permitted by statutory regulation or exceeds the permitted use, you will need to obtain permission directly from the copyright holder. To view a copy of this licence, visit <http://creativecommons.org/licenses/by/4.0/>.

© The Author(s) 2023